Gabbro Discovery in Discovery Deep: First Plutonic Rock Samples From the Red Sea Rift Axis

Jörg Follmann[1]*, Froukje M. van der Zwan[1], Jonas Preine[2], Christian Hübscher[2], Romain Bousquet[3] and Nico Augustin[4]

[1]King Abdullah University of Science and Technology, Thuwal, Saudi Arabia, [2]University of Hamburg, Hamburg, Germany, [3]Christian-Albrechts-University, Kiel, Germany, [4]GEOMAR Helmholtz-Centre for Ocean Research, Kiel, Germany

Plutonic rocks such as gabbros provide information on magmatic and tectonic processes which occur beneath a mid-ocean rift axis as well as on the formation of the oceanic crust. Igneous rocks, reported from the Red Sea Rift valley, have been limited to extrusive basalts so far. The only deeper crustal rocks found in the Red Sea area are from the rift flanks and are interpreted as late-stage continental rift magmatism. Here, we present the geochemistry of the first recovered gabbro fragments from the axis of the Red Sea Rift, sampled from a crater structure within the brine-filled Discovery Deep at the axis of the Red Sea Rift. Petrology and geochemistry show characteristics of a typical mid-ocean ridge gabbro formed at shallow crystallization depth. Clinopyroxene core mineral data fall within two groups, thus pointing to a multiphased magmatic history, including different magma batches and a joint late-stage fractional crystallization. Geobarometry, based on clinopyroxene cores, suggests lower crystallization pressures than similar geobarometric data reported for gabbroic samples from Zabargad (8–9 kbar) and Brother's Islands (2.5–3.5 kbar) at the rift flanks. However, based on the evolved whole rock composition, its multiphase history, the thickness of the crust, the current location of the samples, and the uncertainties in the barometer, geobarometric estimates for the samples are likely overestimated. Instead, we propose that these rock fragments originate from the upper part of a fully developed oceanic crust in the central Red Sea Rift. High-resolution bathymetry and sparker seismic data reveal that the Discovery Deep is characterized by a significant normal fault and a strong reflector near the rift axis, which we interpret as a potential sill intrusion in an approximate depth of 400 m. Based on the lack of progressive alteration and the sampling location within a sediment-free crater structure, we interpret that the emplacement of the gabbros has to be geologically recent. We interpret the gabbro either as a xenolith transported by the eruptive volcanism that formed the crater, potentially related to the sill intrusion visible at depth, or as intrusive gabbro, which was uplifted and deposited in a talus fan by the adjacent normal fault, exposed by the formation of the volcanic crater.

Keywords: gabbro, geochemistry, bathymetry, red sea rift, sparker seismic, oceanic crust

INTRODUCTION

As a main part of the plutonic oceanic crust, gabbros provide essential information about deep crustal processes. However, apart from ophiolites, the accessibility of the lower oceanic crust is limited. Samples from mid-ocean ridges are recovered from sparse drill holes, such as in the Southwest Indian Ridge (Dick et al., 2000), the Mid-Atlantic Ridge (Koepke et al., 2005), the Hess Deep in the eastern central Pacific (Mevel et al., 1996), or at locations of amagmatic exhumation of the deep oceanic crust and/or mantle at oceanic core complexes or exposure of deeper sections along with detachment and transform faults (e.g., MacLeod et al., 2002; Searle et al., 2003). The chances of recovering lower crustal samples from the latter are much higher at slow- and ultraslow spreading ridges due to a low magma supply that dominates tectonic over magmatic processes. Thus, slow- and ultraslow-spreading ridges are key environments to study gabbroic rocks, which hold the potential to help understanding the depth, thermal history, and size of magma reservoirs, as well as to constrain models of basalt differentiation and oceanic crust formation (Meyer et al., 1989).

The geochemistry of these rocks provides essential information about the magmatic processes that occur at the base of the oceanic crust near mid-ocean ridges. Most gabbroic rocks recovered are described as cumulates (e.g., Dostal and Muecke, 1978; Tiezzi and Scott, 1980; Meyer et al., 1989; Ray et al., 2011). Thus, they are interpreted as evidence of the existence of magma reservoirs beneath mid-ocean ridges and contribute to the understanding of crystallization, fractionation, and melt-crystal reaction processes following decompressional mantle melting (Lissenberg and Dick, 2008).

In the Red Sea Rift, no lower crustal or mantle rocks have, so far, been recovered from its ultra-slow spreading rift axis (Chu and Gordon, 1998), potentially as a result of the stronger magmatism in the south caused by the Afar plume (Augustin et al., 2016a). Plutonic samples were only recovered from the rift flanks at Zabargad and Brothers Islands (Bonatti and Seyler, 1987), an off-axis drill hole at 25.5°N (Ligi et al., 2018), and from the continental Tihama Asir complex in southern Saudi Arabia (Ghent et al., 1979; Coleman et al., 1979; Habtoor et al., 2016). Particularly in the Red Sea, where the geology regarding the nature of the crust and its tectonic features is still under debate, information on the deeper crust would be highly relevant for future discussions.

Here, we present the petrology and geochemistry of the first gabbro fragments recovered from the Red Sea Rift axis as well as the local bathymetry and sub-bottom architecture of the sample location at Discovery Deep, constrained from seismic reflection data.

GEOLOGICAL BACKGROUND

The Red Sea Rift is a divergent plate boundary with spreading rates of 16 mm/yr at 18°N to 10 mm/yr at 25.5°N (Chu and Gordon, 1998). Thus, the Red Sea Rift is classified as an ultra-slow spreading rift (Dick et al., 2003). While a fully exposed rift valley

with extensive volcanism influenced by the Afar plume exists in the South (Roeser, 1975; Augustin et al., 2016a), the central Red Sea Rift is characterized by several salt and sediment slumps that blanket large parts of the rift valley (Mitchell et al., 2010; Augustin et al., 2014; Augustin et al., 2021). North of the Zabargad Fracture Zone, the exposed oceanic crust becomes sparser. The age, as well as the extent of the oceanic crust in the northern Red Sea, is still under debate, varying from being in rifting to spreading transition to 13 Ma after the continental breakup (Cochran, 2005; Mitchell and Park, 2014; Ligi et al., 2018; Augustin et al., 2021). While the nature of the crust underneath the sediments remains controversial, the non-blanketed areas of the rift axis show morphological features typical of (ultra) slow-spreading mid-ocean ridges, such as a rift valley, steep faults, rifted volcanoes, and a highly tectonized terrain (Augustin et al., 2016a).

The magma supply of ultra-slow spreading ridges is generally low but shows significant variations, which is highlighted in the Red Sea Rift by the presence of tectonically active areas alternating with large dome volcanoes (Augustin et al., 2016a). The Red Sea Rift shows evidence for volcanic ridges and a large number of volcanic cones and domes in the rift valley of the deeps. These craters between the Erba and Poseidon Deeps in the central Red Sea have a depth of up to 143 m, the larger ones have elevated rims, possibly ejecta from past eruptions (Augustin et al., 2016a). Basalt samples have been recovered from most of the deeps (van der Zwan et al., 2015 and references therein). Several brine-filled depressions are known along the Red Sea Rift (Degens and Ross, 1970; Gurvich, 2006). Some brines are heated up by steady hydrothermal input, leading to almost 70°C as reported in Atlantis II Deep and 45°C in the Discovery Deep (Schmidt et al., 2013).

Mantle rocks and large-scale oceanic core complexes (OCCs), where deep crustal and mantle rocks are exhumed on the seafloor via low-angle detachment faults, are reported from most (ultra-) slow-spreading rifts (e.g., Dick et al., 2003; Escartin et al., 2003) but not yet from the Red Sea Rift. So far, gabbros from the Red Sea area have only been reported from the far off-axis Zabargad and Brothers Islands (e.g., Bonatti and Seyler, 1987; Piccardo et al., 1988) and a borehole on the Nubian side of the rift. Furthermore, lower crust and mantle rocks are exposed on Zabargad island and are associated with uplifted crustal blocks on the western rift flanks. They consist of mantle-derived peridotite, gneisses, amphibolites, metamorphic overprinted pyroxenites, and gabbros (Bonatti and Seyler, 1987). The Zabargad gabbroic rocks and metagabbros show primary (recrystallized) clinopyroxene, orthopyroxene, plagioclase, and amphibole intergrowth with accessory minerals such as zircon, ilmenite, magnetite, and epidote (Bonatti and Seyler, 1987). One gabbroic sample recovered from Zabargad Island shows a quartz-hypersthene-normative composition similar to tholeiitic basalt. However, high Al_2O_3 and CaO contents are interpreted as indications that these rocks are cumulates rather than a complete crystallization of a basaltic liquid (Piccardo et al., 1988). Samples recovered from the gabbroic–doleritic complex on Brothers Island are classified as low-P gabbros, crystallized at <10 km depth as intrusions during thinning and stretching of the continental crust (Bonatti and

Seyler, 1987). The gabbro samples recovered off-axis from a borehole at 25.5°N between the Brothers Island and Zabargad Island provide an $^{40}Ar/^{39}Ar$ age of 25 ± 6 Ma. The Nd isotopic signature of these off-axis samples overlaps with that of the Red Sea oceanic crust and global MORB. Clinopyroxene barometry provides crystallization pressures of 2.5–3.5 kbar. Taking the distance from the rift axis and the spreading velocities in the northern Red Sea into account, these lower crustal rocks are interpreted as intrusions into thinned continental crust followed by exhumation and block rotation during extension, comparable to the uplift of the Zabargad lower crustal rocks (Ligi et al., 2018).

Intrusions of the Jabal Tirf igneous complex on the Arabian continent are also interpreted to be rift related, and with K/Ar ages of 20–24 Ma, these gabbros represent an early stage of rifting and are significantly older than the Red Sea Rift oceanic crust (Coleman et al., 1979). Volcanism on the Arabian plate shows two magmatic phases, an older one from 32 Ma—15 Ma and a younger one starting around 12 Ma and ongoing, both classified as intraplate volcanism (Camp and Robool, 1992).

METHODS

Bathymetry

Multibeam bathymetry data of the sampling areas were collected during expeditions P408 of the German *R/V Poseidon* (Schmidt et al., 2011) as well as 64PE-350/351 and 64PE-445 of the Dutch *R/V Pelagia* (Schmidt et al., 2013; Augustin et al., 2019). *R/V Pelagia* operated a 30 kHz Kongsberg Maritime AS EM302 multibeam system for water depths up to 7,000 m. *R/V Poseidon* was equipped with a hull-mounted ELAC Nautic Seabeam 3,050 echo sounder with a 50 kHz frequency and a maximum working depth of 3,000 m. The digital terrain model (DTM) has a spatial resolution of 30 m, and the grids are publicly available from the PANGAEA data repository (Augustin et al., 2016b; Augustin et al., 2020). Backscatter data from this area were only usable from *R/V Pelagia* 64PE-445 due to poor weather conditions on the earlier expeditions. The backscatter mosaic has a resolution of 30 m (**Supplementary Material 1**). The nomenclature of the Red Sea Deeps used in the text and figures follows the compilation of Augustin et al. (2014) and references therein.

Seismic Data

This study presents one seismic line (64PE-445-18SPS, segment 03) crossing the Discovery Deep derived from a larger dataset collected during expedition 64PE-445 (Augustin et al., 2019). As a seismic source, we used a Delta Sparker system with a dominant frequency of approximately 300 Hz. Seismic energy was recorded using a Microeel solid-state streamer with 24 channels and a length of 100 m resulting in an in-line common-midpoint bin spacing of 8 m. Processing of the seismic data was carried out using VISTA seismic processing software and comprised trace-editing, simple frequency filtering (50–2000 Hz), predictive deconvolution for bubble suppression, followed by NMO correction (1,500 m/s), CMP stacking, finite-difference post-stack migration, as well as top-muting and white noise

removal. Interpretation of the seismic data was carried out using the KingdomSuite software by IHS. For a detailed overview of the method, see Hübscher and Gohl (2014).

Sampling and Bulk Rock Geochemistry

Gabbro samples were recovered with a gravity corer from the Discovery Deep at 21°16.9′N/38°02.7′E (**Figure 1**) in the Red Sea Rift during expedition 64PE-445 SaltAx (August–September 2018) at a water depth of 2,240 m (Augustin et al., 2020). No sediment core was recovered from this station, but an assemblage of hard fragments was caught in the core catcher, consisting of mm-cm sized gabbroic rock and carbonate fragments, shells, iron hydroxides, and aragonite crystals. Some of the carbonate fragments have a manganese coating. From the 13 fragments, the largest pieces were selected for X-ray fluorescence (XRF; 2 fragments), thin section preparation, and electron probe microanalyzer (EPMA) analyses (3 fragments).

Major- and main trace-element concentrations of two gabbro fragments were determined by X-ray fluorescence at the University of Kiel, Germany (**Table 1**). The samples were prepared as two glass tablets, adding 2.4 g $LiBO_4$ to 0.6 g of the pulverized and homogenized sample. Measurements have been performed with a Panalytical Zetium XRF, and the data were automatically internally corrected for spectral overlaps as well as for matrix effects using the De Jongh Alpha calibration model (De Jongh, 1973). Loss on ignition has been determined at 1,100°C and an ignition time of 24 h.

Mineral Chemistry

Major-element concentrations of the main mineral phases olivine (21 crystals), plagioclase (26 crystals), clinopyroxene (28 crystals), and ilmenite (49 crystals) on the three thin section fragments have been measured using a JEOL JXA-8200 electron microprobe at the GEOMAR Helmholtz-Centre for Ocean Research, Kiel, Germany. All minerals have been measured with a beam acceleration voltage of 15 kV. Beam currents of 10 nA for olivine, 20 nA for plagioclase and clinopyroxene, and 50 nA for ilmenite have been used. We used a focused beam for olivine, plagioclase, and oxides and spot sizes of 1 μm for clinopyroxenes. Analytical precision (2σ standard deviation) of the main elements in each silicate phase is <2% for SiO_2, CaO, MgO, and Al_2O_3, <5% for Na_2O and FeO, and <10% for K_2O, TiO_2, and Cr_2O_3. For data quality monitoring and calibration, reference samples from the Smithsonian Institute have been used (Jarosewich et al., 1980) (see supplementary data for accuracy of the standard measurements). All measurements have been performed on fresh, non-poikilitic crystals (**Figure 2**).

RESULTS

Bathymetry & Reflection Seismic Data

The bathymetric maps of the Discovery Deep and surrounding areas reveal numerous volcanic structures, faults, and depressions (**Figures 1B,C**). The Discovery Deep is a semi-circular depression SE of the Atlantis II Deep with a low rugose seafloor, deepening
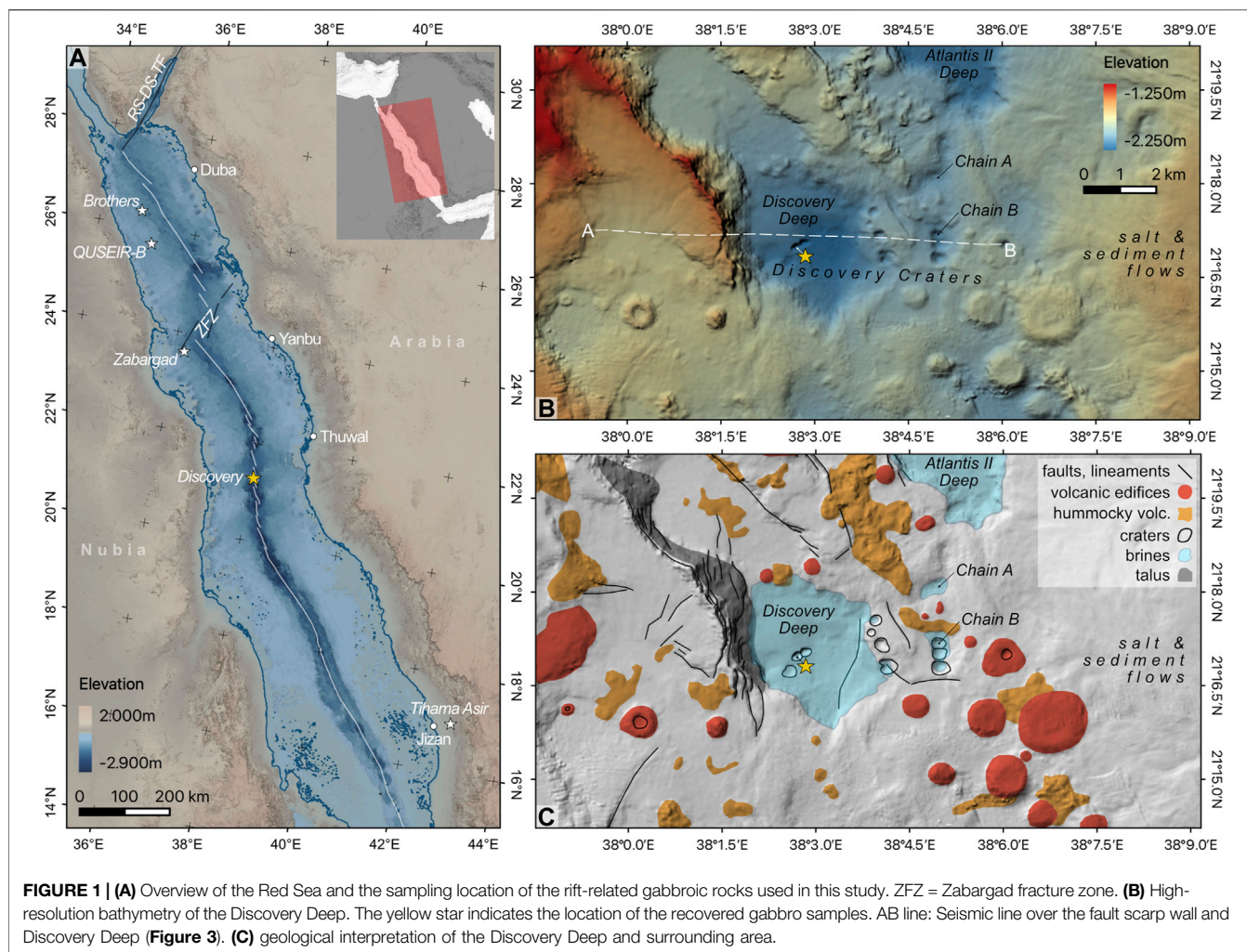
FIGURE 1 | (A) Overview of the Red Sea and the sampling location of the rift-related gabbroic rocks used in this study. ZFZ = Zabargad fracture zone. **(B)** High-resolution bathymetry of the Discovery Deep. The yellow star indicates the location of the recovered gabbro samples. AB line: Seismic line over the fault scarp wall and Discovery Deep (**Figure 3**). **(C)** geological interpretation of the Discovery Deep and surrounding area.

TABLE 1 | XRF bulk rock analyses for gabbroic fragments.

wt%	64PE445_2	64PE445_3	ppm	64PE445_2	64PE445_3
SiO_2	47.76	48.34	Co.	30	34
TiO_2	0.78	0.70	Ni	84	85
Al_2O_3	18.52	17.07	Cr	248	295
Fe_2O_3	8.65	8.59	V	209	190
MnO	0.15	0.15	Ba	21	33
MgO	7.10	7.70	Cu	37	35
CaO	13.16	13.21	Nb	3	2
Na_2O	2.08	2.08	Sr	92	93
K_2O	0.05	0.05	Zr	49	48
P_2O_5	0.07	0.07	Zn	116	95
			La	4	< LLD
LOI	0.64	1.75	Ce	20	14
Total	98.94	99.71			

from north to south with a gentle slope from about 2,200 m to 2,800 m. It is bounded to the west by a significant, east-facing normal fault with an exposed fault scarp of about 680 m and a talus fan that partly extends into the Discovery Deep. The deep has a smooth topography, which is interrupted by large,

oval-shaped, and crater-like depressions. These craters are up to 300 m long, 250 m wide, and 50 m deep (**Figure 1B**). East of the Discovery Deep, two more groups of crater-like depressions are visible, they are aligned N-S and follow the general trend of the Red Sea Rift (chains A and B; **Figures 1B,C**). These craters are up to 500 m wide and 100 m deep, and the crater chains are 1,100 m and 1700 m in length. The Hummocky volcanic terrain is present around the craters as well as a very flat, cratered volcanic edifice further to the east (**Figures 1B,C**). Volcanic edifices and volcanic terrain are abundant around Discovery Deep and the southern part of the Atlantis II Deep, with volcano sizes ranging from 100 m to >3 km in diameter. While most structures are flat-topped volcanoes, we found some volcanoes with craters, in addition to smaller volcanic cones and hummocky volcanic terrain (**Figures 1B,C**). Multibeam backscatter mosaics reveal a relatively even, low backscattering seafloor in the observed area, indicating a sedimented area. Only a few high backscattering patches that may be less sedimented are visible in the data within the Discovery Deep (not related to apparent bathymetric features). Further visible are the main fault and the talus fan, and other fault scarps are visible in the data (see **Supplementary Appendix 1**).

FIGURE 2 | **(A)** Recovered fresh gabbroic rock fragments. Squares in the background are 1 cm. Thin section of one gabbro fragment in **(B)** plane-polarized light and **(C)** cross-polarized light.

The internal architecture of the Discovery Deep is revealed by the seismic profile illustrated in **Figure 3A**. This line crosses the distinct east-facing escarpment and traverses the Discovery Deep slightly north of the central craters before crossing the craters observed east of the Deep (**Figure 1B**). The seismic line is generally characterized by a thin sequence of layered
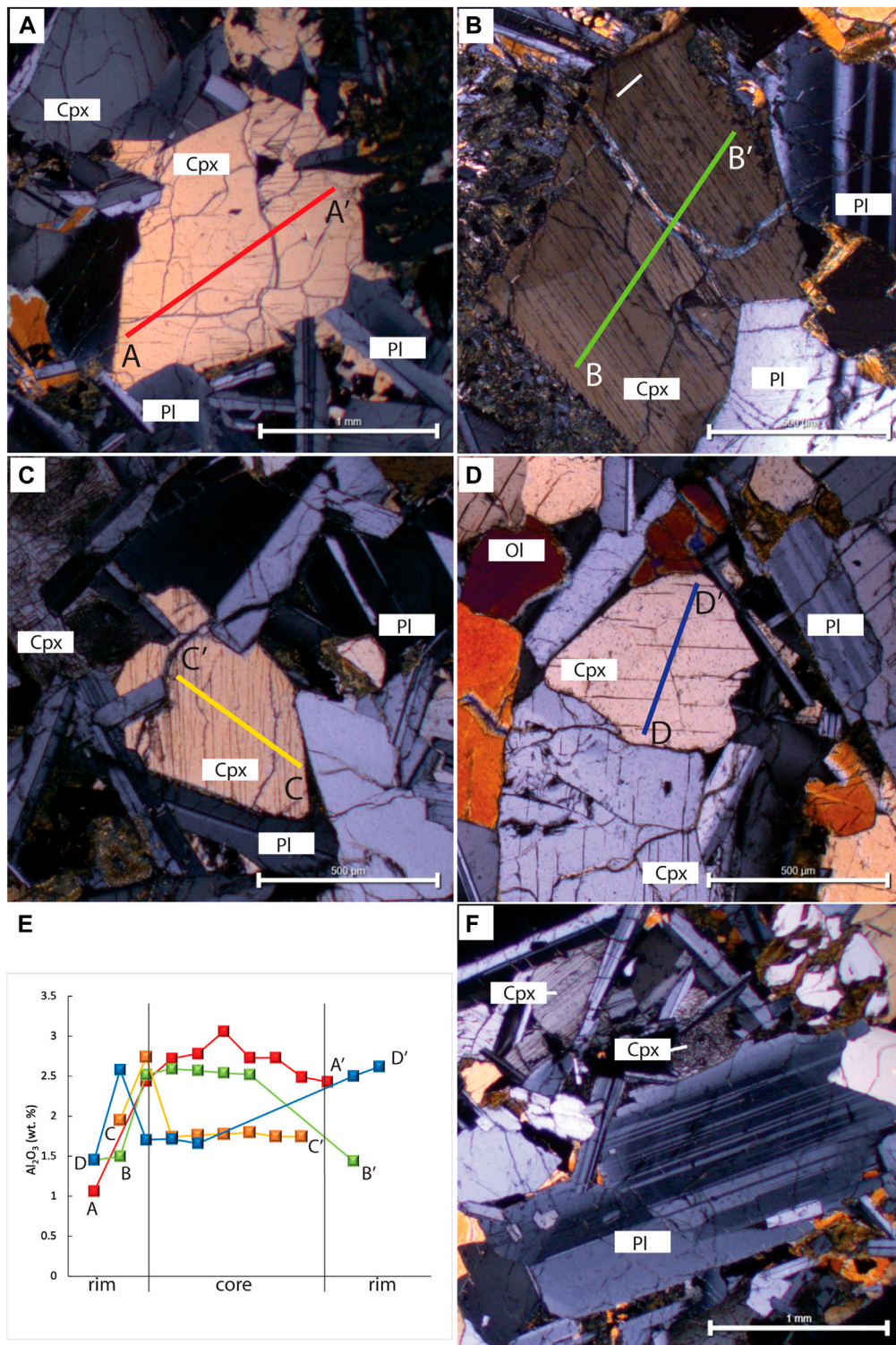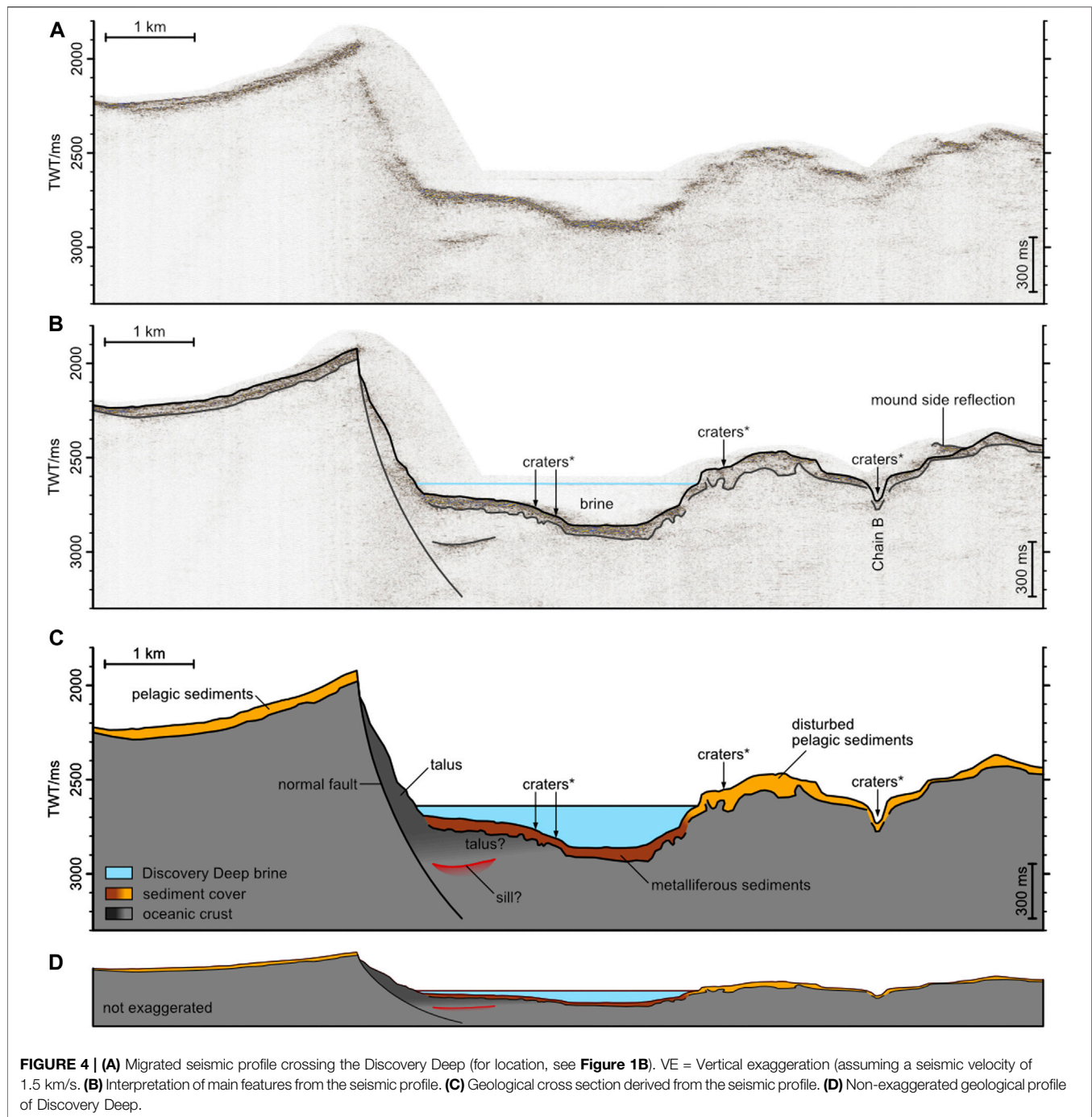
FIGURE 3 | (A,B): Clinopyroxene crystals from the high aluminum group. **(C,D)**: Clinopyroxene crystals from the low aluminum group. **(E)**: Mineral chemistry plots of Al_2O_3 (wt%) over the profiles for the four clinopyroxene crystals **(A-D)**. **(F)**: Large plagioclase crystal visible is a concentric zonation.

FIGURE 4 | (A) Migrated seismic profile crossing the Discovery Deep (for location, see **Figure 1B**). VE = Vertical exaggeration (assuming a seismic velocity of 1.5 km/s. **(B)** Interpretation of main features from the seismic profile. **(C)** Geological cross section derived from the seismic profile. **(D)** Non-exaggerated geological profile of Discovery Deep.
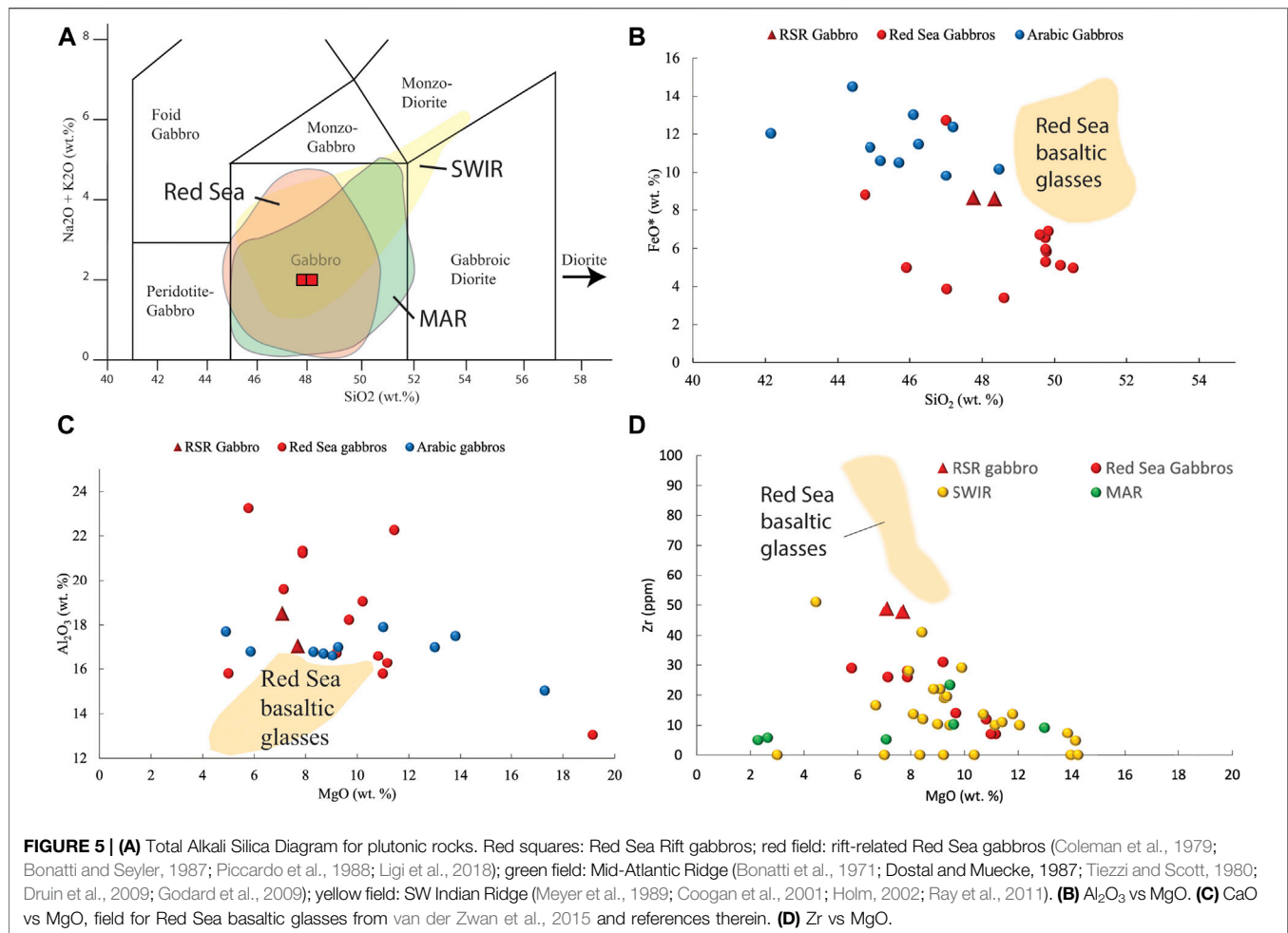
reflections above the acoustic basement. This upper sequence has higher amplitudes in Discovery Deep compared to the low-amplitude sequence west of the Deep. Towards the east, we observed that this upper unit becomes more chaotic above a hummocky acoustic basement. Above the Discovery Deep, we identify a subtle horizontal reflection at 100–200 ms two-way travel time (TWT) above the seafloor and corresponds to the high-salinity brine. In addition to that, we detected a prominent

concave reflection on the hanging wall of the fault that loses expression west of the projected location of the craters **Figure 4**).

Petrography

Thirteen gabbro fragments were collected, ranging in size from 0.5 to 2.5 cm (**Figure 2A**). All fragments look in hand specimen very similar, and none of the gabbro samples had any type of coating or encrustations, such as basalt, manganese, or an alteration layer.

FIGURE 5 | (A) Total Alkali Silica Diagram for plutonic rocks. Red squares: Red Sea Rift gabbros; red field: rift-related Red Sea gabbros (Coleman et al., 1979; Bonatti and Seyler, 1987; Piccardo et al., 1988; Ligi et al., 2018); green field: Mid-Atlantic Ridge (Bonatti et al., 1971; Dostal and Muecke, 1987; Tiezzi and Scott, 1980; Druin et al., 2009; Godard et al., 2009); yellow field: SW Indian Ridge (Meyer et al., 1989; Coogan et al., 2001; Holm, 2002; Ray et al., 2011). **(B)** Al_2O_3 vs MgO. **(C)** CaO vs MgO, field for Red Sea basaltic glasses from van der Zwan et al., 2015 and references therein. **(D)** Zr vs MgO.

Thin sections of the studied gabbro fragments consist of approximately 95% fresh minerals (**Figures 2A,B**) and show the ophitic texture of the rock. Plagioclase has a modal proportion of 45 vol% with large, prismatic, subhedral crystals, ranging in size from 0.5–2.5 mm and showing albite twinning and concentric zoning. Some plagioclase crystals show a poikilitic texture with a chadacryst phase that is too fine-grained to be identifiable. A few plagioclases are rich in fluid inclusions. Clinopyroxene crystals (35 vol%) range from 0.4–1.3 mm in size and are subhedral to euhedral, intergrown with plagioclase. Orthopyroxene and transparent spinel each constitute a minor proportion of 5 vol %. Olivine crystals (5 vol%) mostly show sizes in the range from 0.2 to 0.5 mm, with few crystals that reach 1 mm. Hence, the olivine crystals are smaller than both plagioclases and pyroxenes and either fill the intergranular space between these major phases or occur as inclusions in clinopyroxenes. Olivines are anhedral to subhedral and are free of serpentinization. However, most olivine crystals show a corona of dissolution, possibly altered to iddingsite. Opaque oxide minerals are accessory and randomly distributed but mainly associated with brownish, fine-grained patches of mixed unidentified alteration minerals with a combined proportion of 5 vol%.

Bulk-Rock Chemistry

The rock fragments have LOIs of 0.64 and 1.75 wt% and a bulk rock Mg# (Mg# = Mg/(Mg + Fe)) of 0.45 and 0.47. The content of alkalis ($K_2O + Na_2O$) is 2.13 wt% (**Figure 5A**) for both measured fragments, and thus, the samples fall within the geochemical field defined for gabbros in the total alkali-silica diagram (Middlemost, 1994). Al_2O_3 shows variations of 18.5 and 17.1 wt% for the two fragments. FeO concentrations in the newly described rocks are within the range of other Red Sea gabbros (<9 wt%) and lower than reported samples from the Tihama Asir complex 10–15 wt %) (**Figure 5B**). All rift-related gabbro data included in this study show Al_2O_3 concentrations in the range of 13–23 wt%. The bulk rock chemistry of the two gabbro samples shows higher Al_2O_3 and lower SiO_2 concentrations than basaltic glasses from the rift axis but mostly overlap for other major elements (**Figure 5C**).

Trace element concentrations of the gabbros are generally low and in the same range as the samples from the northern Red Sea (Zabargad Island (Bonatti and Seyler, 1987; Piccardo et al., 1988), Brothers and QUSEIR gabbro (Ligi et al., 2018), and the Tihama Asir gabbros (Ghent et al., 1979). Compatible elements incorporated in the main silicate phases (Ni, Cr) show higher concentrations, and Sr is elevated due to the compatibility in
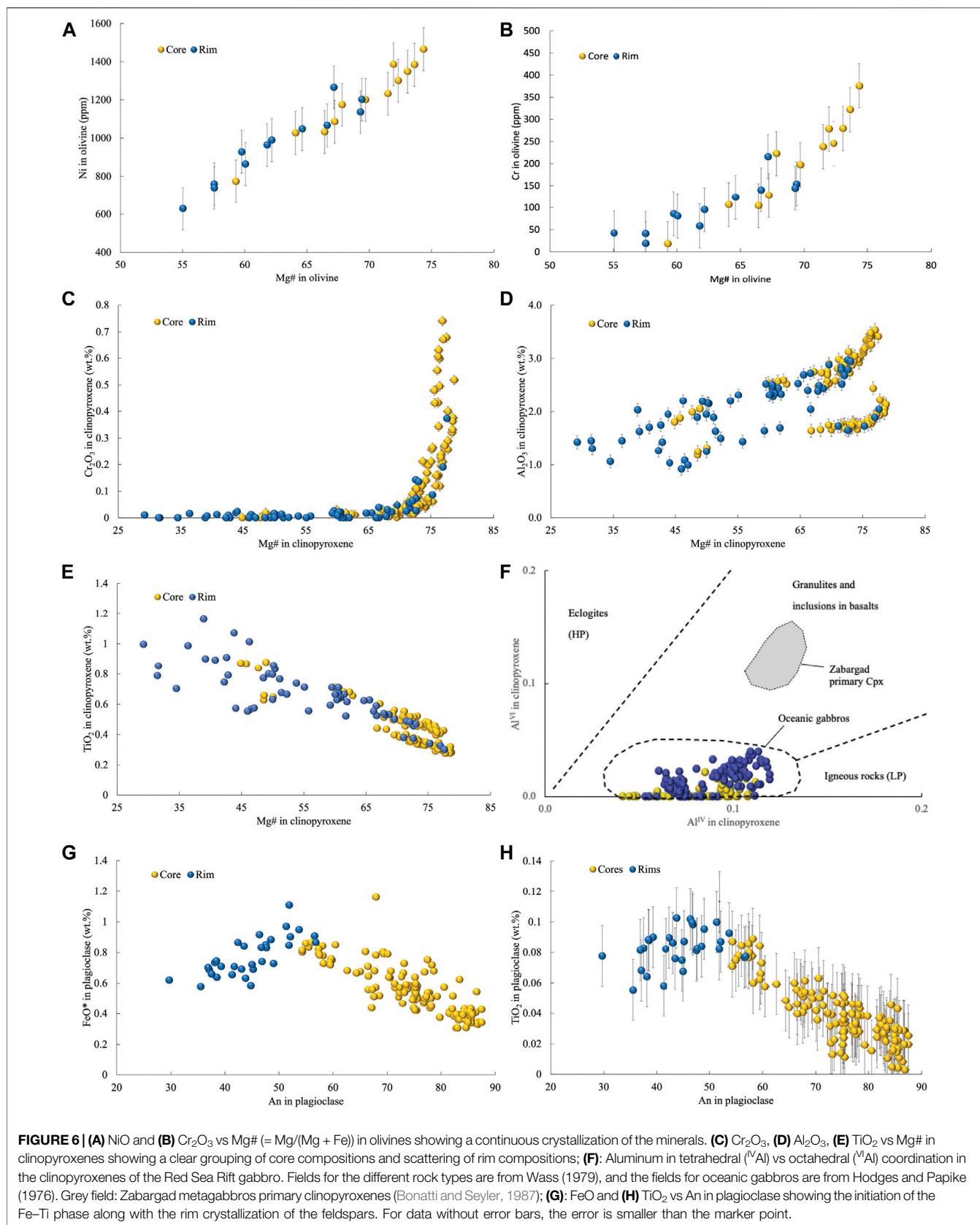
FIGURE 6 | (A) NiO and **(B)** Cr_2O_3 vs Mg# (= Mg/(Mg + Fe)) in olivines showing a continuous crystallization of the minerals. **(C)** Cr_2O_3, **(D)** Al_2O_3, **(E)** TiO_2 vs Mg# in clinopyroxenes showing a clear grouping of core compositions and scattering of rim compositions; **(F)**: Aluminum in tetrahedral (^{IV}Al) vs octahedral (^{VI}Al) coordination in the clinopyroxenes of the Red Sea Rift gabbro. Fields for the different rock types are from Wass (1979), and the fields for oceanic gabbros are from Hodges and Papike (1976). Grey field: Zabargad metagabbros primary clinopyroxenes (Bonatti and Seyler, 1987); **(G)**: FeO and **(H)** TiO_2 vs An in plagioclase showing the initiation of the Fe–Ti phase along with the rim crystallization of the feldspars. For data without error bars, the error is smaller than the marker point.

TABLE 2 | Representative EPMA measurements of the main mineral phases olivine (Ol), clinopyroxene (Cpx), pop. 1 = population 1, high Al_2O_3, Cr_2O_3, TiO_2 group, pop. 2 = population 2, low Al_2O_3, Cr_2O_3, TiO_2 group, plagioclase (Plag), and Ilmenite (Ilm). All numbers in wt%.

	Ol core	Ol rim	Cpx core pop. 1	Cpx core pop. 2	Cpx rim	Plag core	Plag rim	Ilm
SiO_2	40.21	39.30	52.01	52.89	51.75	51.36	59.32	0.12
TiO_2			0.454	0.362	0.555			20.270
Al_2O_3	0.029	0.022	2.870	1.729	1.860	30.310	25.300	1.980
FeO	15.66	22.26	6.28	6.69	9.72	0.57	0.66	74.75
MnO	0.259	0.350	0.179	0.169	0.273			0.529
MgO	44.29	38.66	17.22	17.95	16.42	0.19	0.05	0.88
CaO	0.38	0.36	20.73	20.14	18.89	13.63	7.48	
Na_2O			0.227	0.222	0.276	3.550	6.830	
K_2O			0.000	0.006	0.013	0.021	0.076	
Cr_2O_3	0.024	0.004	0.097	0.043	0.013			0.033
Total	100.99	101.04	100.09	100.22	99.79	99.68	99.79	98.58

plagioclase. The Zr is with 49 and 48 ppm in the two fragments and thus enriched relative to the gabbro analyses from the Mid-Atlantic Ridge (Miyashiro et al., 1970; Bonatti et al., 1971; Dostal and Muecke, 1978; Tiezzi and Scott, 1980; Drouin et al., 2009; Chen et al., 2013) or SW Indian Ridge (Meyer et al., 1989; Coogan et al., 2001; Holm, 2002; Ray et al., 2011).

Mineral Chemistry

Olivine crystals show a normal zonation with cores of on average Fo_{80} and rims of on average Fo_{73}. The Ni and Cr contents show a positive correlation with the Fo content of the crystals (**Figures 6A,B**). Hence, both elements are more concentrated in the cores (774–1,465 ppm NiO, 18–376 ppm Cr_2O_3) than in the rims (629–1,266 ppm NiO, 19–216 ppm Cr_2O_3). In contrast, Mn concentrations increase towards the rims up to 6,130 ppm. The plagioclase also show a zonation, with An-rich cores (An_{76}) and Na-richer compositions (An_{44}) towards the rims. From the core to rim, FeO and TiO_2 increase with decreasing An content followed by a decrease in FeO, TiO_2, and An in the rim measurements (**Figures 6G,H**). Measurements have been performed on fresh, non-poikilitic crystals. Representative measurements for the main mineral phases are documented in **Table 2**.

All measured clinopyroxenes have been classified as augites by stoichiometry. Mg numbers (Mg# = Mg/(Mg + Fe)) ranging from 78.7 to 29.2, indicating a normal zonation. Crystal cores are FeO-poor (av. 7.3 wt%) with increasing FeO-concentrations towards the rims (av. 12.7 wt%) along with an enrichment of MnO and TiO_2 and a decrease in Al_2O_3, Cr_2O_3, NiO, and CaO (**Figures 6A–E**). The Cr_2O_3 concentrations in clinopyroxenes decrease exponentially with decreasing Mg#, from 0.82 wt% to below detection limit (**Figure 6D**). Aluminum in clinopyroxene generally shows higher concentrations in the cores (**Figure 6D**). Two distinct groups of clinopyroxene core compositions are visible in Al_2O_3, TiO_2, and Cr_2O_3, one with higher and one with lower concentrations of these oxides. This grouping is mainly visible in the core measurements and is less marked in the rim compositions (**Figure 6E**). The two distinct groups appear in all three fragments and are not related to mineral size, particular neighbor minerals, areas on the section, or

analytical issues but occur throughout consistently throughout the thin sections and are larger than the analytical error (see error bars in **Figure 6**).

The distribution of Al^{VI}/Al^{IV} (**Figure 6F**) in the clinopyroxenes, calculated from the stoichiometric formulas shows that our measured clinopyroxenes are clearly distinct from the Al values of the primary clinopyroxene in the Zabargad metagabbros but fit very well with the oceanic gabbro field from Hodges and Papike (1976).

The measured intergrown opaque minerals are Fe–Ti oxides, with a TiO_2 concentration of 10–25 wt% and therefore classified as ilmenites.

DISCUSSION

Emplacement of the Gabbro

The gabbro fragments from the Discovery Deep are the first ones that have been recovered from the Red Sea rift axis. No other deeper crustal rocks have been found so close to the rift axis before, despite its slow-spreading character, which was earlier attributed to higher volcanic activity related to the Afar plume (Augustin et al., 2016b). The samples studied in this publication were not recovered from a core complex but instead from a crater structure with a limited sediment cover. The sampled craters also show a stronger backscatter signal (**Supplementary Appendix 1**) than the surrounding deeper parts of the surveyed area, possibly as a result of coarser talus or erupted material with little or no sediment cover (e.g., Hewitt et al., 2010). Even though most parts of the deep are filled with metalliferous sediments (Gurvich, 2006), no sediments were recovered during the sampling (Augustin et al., 2020). Hence, the crater appears to be sediment-free, even though located in a largely sedimented, brine-filled depression. Eruption craters have been observed in the Red Sea Rift in several areas usually covered by evaporites and sediments (e.g., between the Erba and Poseidon Deeps). Based on their morphology and location within the neovolcanic zone, these eruptive craters have been classified as volcanic craters (see Augustin et al., 2016a for a detailed discussion). Although the craters in Discovery Deep have a slightly higher depth/width ratio

compared to the other Red Sea craters, their morphology, the roundness of the crater, the lack of sedimentary muds, and also their location in the neovolcanic zone (supported by the mid-ocean ridge geomorphology in the study area) point to a similar origin (**Figures 1B,C**). The possibility of (explosive) eruptions in the deeper marine settings, as is necessary to create such craters, is rather new and poorly understood but has also been introduced for the Charles Darwin Volcanic Field, Cape Verdes (Kwasnitschka et al., 2013), and for a monogenetic volcano field on the Southwest Indian Ridge (Dick, 2021).

Figures 3B–D illustrate the information obtained from the seismic line crossing the Discovery Deep, slightly north of the crater. This interpretation is based on the described seismic facies and on the geological map shown in **Figure 1C**. We interpret the stratified sequence on top of the acoustic basement as pelagic sediments. The higher-amplitude apron within the deep is likely metalliferous sediments, as was indicated by extensive ground-truthing (Gurvich 2006). Furthermore, the eastward dipping normal fault can be traced to depth with a talus fan extending from the fault, potentially up to the location of the craters. The visible concave reflection underneath the approximate location of the craters fulfills the criteria defined by Planke et al. (2005) for the interpretation of seismic events as sill reflections: it is 1) of high amplitude, has 2) a saucer-shape, and 3) terminates abruptly. We approximate the depth of this potential sill to be 400 m below the sea floor level (assuming a seismic velocity of approximately 3 km/s). This sill could potentially have provided a magma and/or heat source for the eruptive craters, but based on the seismic line, we do not see a reflector that could indicate a feeder dike from the sill to the craters. The absence of such a steep dipped feeder dike in the seismic image could be result of the limited vertical resolution, caused by the short streamer length of only 100 m. On the other hand, concerning the complex three-dimensional shape of a sill intrusion and the position of the seismic line that is slightly north of the crater structures, the displayed profile could be out of plane to provide evidence for a feeder from the potential intrusion to the crater.

The interpretation of the crater as a volcanic eruption crater could indicate a volcanic emplacement of the gabbro fragments by the eruption that formed the crater. If the sill was the driving mechanism to form the crater structures on the seafloor, we would expect it to form in an early phase of the intrusion due to the excess of heat (and melt) rather than in a later stage where progressive cooling of the intruded material takes place. So, unless the sill continues to the surface at the crater, it is unlikely that the gabbro directly represents the cooled sill itself. More likely, deeper crustal rocks could be transported to the surface as xenoliths that are typically found in volcanic craters. The absence of host basalt attached to the gabbros, which may seem inconsistent with this hypothesis, could be explained by the fact that the collected fragments are derived from a reasonably large xenolith (consistent with the homogenous appearance and chemistry of the fragments) and/or the occurrence of a more phreatic explosion rather than a phreatomagmatic eruption. Due to our unusual sampling method with a gravity core of only 12.5 cm diameter, we cannot confirm or exclude the presence of basalt.

Alternatively, the gabbros could represent expelled material already in place from the talus fan potentially uplifted by the normal fault or a combination of these two mechanisms. We have no indications of when the exposure took place. However, the lack of hydrothermal alteration despite exposure to the 45°C temperature, high-salinity brine, as well as the lack of sediment coverage in an area with high sedimentation rates (up to 10 cm/kyr; Stoffers and Ross, 1974) point to a rather recent nature of the craters. Therefore, both the uplift of the gabbroic material by a fault and the eruption as a xenolith from larger depth or even a combination of the two are possible scenarios for the emplacement of the gabbro fragments. More detailed investigations of the crater, the talus, and the fault would be needed to distinguish between these scenarios.

Formation History and Crystallization Depth of the Gabbro

The rock fragments overlap in major- and trace-element chemistry with gabbros found at the Mid-Atlantic Ridge and the Southwest Indian Ridge (Dostal and Muecke, 1978; Meyer et al., 1989; Coogan et al., 2001; Holm, 2002; Drouin et, al., 2009; Godard et al., 2009). Considering the grain size of 0.5–2.5 mm, the samples can be classified as a typical mid-ocean ridge gabbro, indicating a slower cooling and crystallization of the fragments at greater depths before exposure of the fragments at the surface where they were sampled. Significant chemical or petrographic differences between the studied fragments have not been observed. The fragments show a chemical overlap with measurements from axial MORB basalts in the Red Sea, and we do not see evidence for continental crustal contamination. The elevated content of Zr, which is incompatible in most mafic-ultramafic systems, compared to gabbros from other slow-spreading ridges along with the low Mg# suggests the Red Sea Rift gabbros to be relatively evolved. Thus, we suggest that the gabbros originate from an asthenospheric melt, which ascends beneath the Red Sea Rift but undergone significant crystallization, which formed the more evolved composition.

The petrography (e.g., olivine inclusions in clinopyroxene and plagioclase) suggests an early crystallization of olivine. The fact that these minerals are smaller than the Pls and Cpx even though they crystallized earlier indicates a termination of olivine crystallization. Recrystallization of olivine, which would also lead to smaller crystal sizes, would equilibrate the element budget of the olivines instead of the typical fractional crystallization of Ni and Cr vs #Mg patterns that we observe here (**Figures 6A,B**), as experimental (Grove and Bryan, 1983) and empirical studies of phenocrysts (Stakes et al., 1984) have shown. Some olivines are entirely altered, as is made apparent by the subhedral to euhedral relict olivine pseudomorph shapes that are filled with alteration products. The intergrowth and similar crystal size range of the two main mineral phases plagioclase and clinopyroxene suggest that they co-formed. The enrichment of FeO and TiO_2 during the crystallization of the plagioclase cores and the trend inflection at around An_{52} indicates the onset of the intergranular ilmenite crystallization to have taken place

simultaneously to the formation of plagioclase rims (**Figures 6G,H**).

The grouping of the core chemistries of clinopyroxenes (observed in 24 crystals), visible in Cr_2O_3, Al_2O_3, and TiO_2, indicates the crystallization of clinopyroxene from different magma batches. The later rim crystallization appears to have happened in one environment, as the rim measurements are scattered and do not follow the core chemistry grouping. Neither the cores nor the rims of the clinopyroxene are in equilibrium with the whole rock chemistry, based on the Fe–Mg partitioning that has K_d $(Fe-Mg)^{cpx-liq}$ values (equilibrium between clinopyroxene and a nominal coexisting liquid) of 0.26–1.22 for cores and 0.24–1.99 for rims, which is significantly higher than the equilibrium values of 0.27 ± 0.03 (Putirka, 1996). The clinopyroxenes of different geochemical groups do not translate into different fragments or noticeable heterogeneities in the recovered gabbros. Therefore, a formation in a single, heterogenous magma reservoir with either local or temporal changes, implying significant small-scale differences in the reservoir's element budget, seems unlikely. Hence, crystallization thus occurred in at least two different environments and under disequilibrium conditions, which implies a history with multiple magma batches and/or melt reactions rather than simple crystallization in one magma reservoir.

A trend towards lower bulk rock Mg# along with a decrease of An in plagioclase, Mg# in clinopyroxene, and Fo in olivine has also been described for shallow gabbros from Hole 735B, interpreted as a progressive upwards differentiation within the crust (Boulanger et al., 2020). Furthermore, a similar trend in FeO vs An content in plagioclase has been reported from Hole 735B at the SW Indian Ridge (SWIR; Dick et al., 2002). Our plagioclase compositions also show an enrichment in FeO with a decrease in An content and with progressive crystallization from core to rim, followed by a decrease in FeO at An contents of An_{55} (Dick et al., 2002). The similarity of the trends in SWIR and the Red Sea rift gabbros may imply that, equally as the SWIR gabbros, our samples were likely formed by crystallization in a mush with a change to an iron–titanium-rich environment in the last stages, as inferred from ilmenite formation. Dick et al. (2002) interpreted such an evolution as a migration of late iron-titanium-rich liquids into fractures in the upper part of the sequence. This is not observed in our samples. As we also see the joining of the two different groups of clinopyroxene at this stage, we interpret that processes such as the mobilization of the crystal mush and mush or magma mixing could have played a role.

Formation Depth of the Gabbros and Relation to the Red Sea

For the off-axis gabbroic samples in the Red Sea, crystallization pressures have been determined using the methods of Nimis et al. (1999), which gives values of 2.8 ± 0.12 kbar and 3.0 ± 0.26 kbar (Ligi et al., 2018). Using the same methods, typical values for temperature input (Soesoo, 1997), comparable petrographic assemblages from the SWIR (Ozava et al., 1991) and the calibration for tholeiitic series. Pressure estimations after

Putirka et al. (1996) calculations fall in the same range with pressures from 1.0 to 5.0 kbar, though most data points fall between 2.0 and 4.1 kbar. In both cases, the calculations only work for the core compositions, not for the rims that are far out of equilibrium with a nominal coexisting fluid. However, both barometer models are calibrated based on extrusive samples rather than gabbroic rocks and require equilibrium conditions, which is not entirely the case. Therefore, these methods provide only first-order information on the depth. Thus, while the crystallization pressures are likely lower than for the off-axis samples, the absolute values may be off. Assuming an oceanic crustal thickness of 5–10 km (Rihm et al., 1991), these crystallization pressures would indicate mid-lower crustal to mantle depths. However, the comparably evolved nature of samples from the Atlantis Bank, SWIR occura in depths of >400 m below the seafloor (Boulanger, 2020) and thus imply a crystallization of the Red Sea gabbro fragments in a shallow magma reservoir—consistent with the estimated depth of the sill intrusion. Considering the constraints from the geochemistry and the comparisons with gabbros from other slow-spreading ridges, the barometer calculations' uncertainty, and the models' limitations for these types of disequilibrium plutonic rocks, it is likely that the pressure calculations are overestimated. We therefore conclude that these gabbros likely occurred within the upper part of the oceanic crust. The coordination of aluminum in the clinopyroxene (**Figure 6F**), a pressure-sensitive proxy, supports the samples to be 'regular' oceanic gabbros, forming in a low-pressure environment.

Based on their distance from the rift axis, spreading velocities, and geobarometric estimations, Zabargad (8–9 kbar) gabbros were interpreted as being formed by underplating and gabbros from Brothers Islands (2.5–3.5 kbar) as shallow intrusions into a progressively thinned continental crust (Bonatti and Seyler, 1987; Ligi et al., 2018). The off-axis samples from Brothers Island and the QUSEIR drill hole show a wide range of similarities with our samples in chemistry, all lacking evidence for contamination with continental lithosphere. Pressure calculations for Brothers Island match with our numerical clinopyroxene estimations (Bonatti and Seyler, 1987), but these are affected by the same limitations as we faced. This could be a similar oceanic crustal origin for those samples, which would support studies that argue for a more comprehensive extension of oceanic crust in the central and northern Red Sea (Sultan et al., 1992; Augustin et al., 2021). On the other hand, the Red Sea Rift gabbros show a significantly lower Al^{VI} proportion than primary clinopyroxene from Zabargad Island. This suggests lower crystallization pressures for the rift axis gabbros and could suggest a transitional stage between oceanic crust and continental rifting.

CONCLUSION

The first gabbroic rock fragments have been recovered from the Discovery Deep at the Red Sea Rift axis. In contrast to other gabbro occurrences from mid-ocean ridges, these samples were not exposed to the surface by core complexes or faults but are likely related to eruptive volcanism. The samples were collected

from a sediment-free crater in a high-salinity brine. Sparker reflection seismic reveals the internal architecture of the Discovery Deep with a strong reflector approximately 400 m below the seafloor that we interpret as a sill intrusion potentially related to the crater structures. This sill can be the source of the eruptive volcanism. Thus, the emplacement mechanism of the gabbros is either as xenoliths, directly associated with volcanism, or the indirect exposure of talus material related to the eruption.

The geochemistry shows that these fragments are typical mid-ocean ridge gabbros with a multiple-stage magmatic history. The early stage is represented by clinopyroxene crystallization in two different magma/mush batches, followed by the crystallization in a late-stage iron–titanium-rich interstitial melt. Pressure calculations using clinopyroxene chemistry suggest crystallization depths of 6–10 km but are likely overestimated, as indicated by the disequilibrium of the minerals. Instead, we suggest a shallow crystallization depth based on petrographic observations, the rather evolved nature of the gabbros, the mineral chemistry, and the current location of the gabbros. These gabbros provide the first insights into the subsurface of the oceanic crust of the Red Sea.

DATA AVAILABILITY STATEMENT

The original contributions presented in the study are included in the article/**Supplementary Materials**; further inquiries can be directed to the corresponding author.

AUTHOR CONTRIBUTIONS

JF and FZ worked out the petrology and geochemistry, visualized these aspects, and worked out the final manuscript. FZ was responsible for the seafloor sampling during cruise 64PE445. JP and CH were responsible for the collection, visualization, and interpretation of the seismic data as well as contributed to the manuscript. RB, FZ, and JF performed the geochemistry analyses. NA and FZ designed the study. NA led expedition 64PE445, interpreted the bathymetric data and contributed to the manuscript.

FUNDING

ACKNOWLEDGMENTS

SUPPLEMENTARY MATERIAL

The Supplementary Material for this article can be found online at: https://www.frontiersin.org/articles/10.3389/feart.2021.742815/full#supplementary-material

REFERENCES

Augustin, N., Devey, C. W., and van der Zwan, F. M. (2019). "A Modern View on the Red Sea Rift: Tectonics, Volcanism and Salt Blankets," in *Geological Setting, Palaeoenvironment and Archaeology of the Red Sea*. Editors N. Rasul and I. Steward (Cham: Springer), 37–52. doi:10.1007/978-3-319-99408-6_3

Augustin, N., Devey, C. W., van der Zwan, F. M., Feldens, P., Tominaga, M., Bantan, R. A., et al. (2014). The Rifting to Spreading Transition in the Red Sea. *Earth Planet. Sci. Lett.* 395, 217–230. doi:10.1016/j.epsl.2014.03.047

Augustin, N., Feldens, P., Kwasnitschka, T., Schmidt, M., Al Farawati, R., and Basaham, A. S. (2016b). High Resolution Bathymetry of the Red Sea Rift (1 Arc-Second) from POSEIDON Cruise POS408 and PELAGIA Cruises 64PE350 and 64PE351. *PANGAEA*. Dataset #860374. doi:10.1594/PANGAEA.860374

Augustin, N., van der Zwan, F. M., Devey, C. W., Ligi, M., Kwasnitschka, T., Feldens, P., et al. (2016a). Geomorphology of the central Red Sea Rift: Determining Spreading Processes. *Geomorphology* 274, 162–179. doi:10.1016/j.geomorph.2016.08.028

Augustin, N., Wölfl, A.-C., Schade, M., van der Zwan, F. M., and Mitchell, N. C. (2020). High Resolution Bathymetry of the Red Sea Rift from PELAGIA Cruise PE445, SALTAX. *GEOMAR – Helmholtz Centre Ocean Res. Kiel, PANGAEA*. Dataset #91278. doi:10.1594/PANGAEA.912178

Augustin, N., van der Zwan, F. M., Devey, C. W., and Brandsdottir, B. (2021). 13 million years of seafloor spreading throughout the Red Sea Basin. *Nat. Comm.* 12. doi:10.1038/s41467-021-22586-2

Bonatti, E., Honnorez, J., and Ferrara, G. (1971). Peridotite-Gabbro-Basalt Complex from the Equatorial Mid-Atlantic Ridge. *Phil. Trans. Roy. Soc. Lond.* 268, 385–402.

Bonatti, E., and Seyler, M. (1987). Crustal Underplating and Evolution in the Red Sea Rift: Uplifted Gabbro/Gneiss Crustal Complexes on Zabargad and Brothers Islands. *J. Geophys. Res.* 92 (B12), 803–812. doi:10.1029/jb092ib12p12803

Boulanger, M., France, L., Deans, J. R. L., Ferrando, C., Lissenberg, C. J., and von der Handt, A. (2020). Magma Reservoir Formation and Evolution at a Slow-Spreading Center (Atlantis Bank, Southwest Indian Ridge). *Front. Earth Sci.* 8, 554598. doi:10.3389/feart.2020.554598

Camp, V. E., and Roobol, M. J. (1992). Upwelling Asthenosphere Beneath Western Arabia and its Regional Implications. *J. Geophys. Res.* 97 (B11), 15225–15271. doi:10.1029/92jb00943

Chen, Z.-Q., Zhou, H.-Y., Liu, Y., Yang, Q.-H., Li, J.-W., and Dick, H. J. B. (2013). Influence of Igneous Processes and Serpentinization on Geochemistry of the Logatchev Massif Harzburgites (14°45′N, Mid-Atlantic Ridge), and Comparison with Global Abyssal Peridotites. *Int. Geology Rev.* 55 (1), 115–130. doi:10.1080/00206814.2012.704674

Chu, D., and Gordon, R. G. (1998). Current Plate Motions Across the Red Sea. *Geophys. J. Int.* 135 (2), 313–328. doi:10.1046/j.1365-246x.1998.00658.x

Cochran, J. R. (2005). Northern Red Sea: Nucleation of an Oceanic Spreading Center Within a Continental Rift. *Geochem. Geophys. Geosys.* 6 (3). doi:10.1029/2004gc000826

Coleman, R. G., Hadley, D. G., Fleck, R. G., Hedge, C. T., Donato, M. M., and Convenor, A. M. (1979). "The Miocene Tihama Asir Ophiolite and its Bearing on the Opening of the Red Sea," in *Evolution and Mineralization of the Arabian-Nubian Shield*. Editor A.M. C Al-Shanti (Oxford: Oxford Pergamon Press Ltd.), 1, 173–186. doi:10.1016/b978-0-08-024460-0.50021-6

Coogan, L. A., MacLeod, C. J., Dick, H. J. B., Edwards, S. J., Kvassnes, A., Natland, J. H., et al. (2001). Whole-Rock Geochemistry of Gabbros from the Southwest Indian Ridge: Constraints on Geochemical Fractionations between the Upper and Lower Oceanic Crust and Magma Chamber Processes at (Very) Slow-Spreading Ridges. *Chem. Geology* 178 (1-4), 1–22. doi:10.1016/s0009-2541(00)00424-1

De Jongh, W. K. (1973). X-ray Fluorescence Analysis Applying Theoretical Matrix Corrections. Stainless Steel. *X-Ray Spectrom.X-ray Spectrosc.* 2 (4), 151–158. doi:10.1002/xrs.1300020404

Degens, E. T., and Ross, D. A. (1970). The Red Sea Hot Brines. *Sci. Am.* 222 (4), 32–42. doi:10.1038/scientificamerican0470-32

Dick, H. J. B. (2021). *An Explosive Monogenetic Alkaline Volcanic Field on the SW Indian Ridge*. Lyon: Goldschmidt Conference.

Dick, H. J. B., Ozawa, K., Meyer, P. S., Niu, Y., Robinson, P. T., Constantin, M., Hebert, R., Maeda, J., Natland, J. H., Hirth, J. G., and Mackle, S. M. (2002). "Primary Silicate Melt Chemistry of a 1.5-km Section of Very Slow Spreading Lower Oceanic Crust: ODP Hole 735B, Southwest Indian Ridge," in Proceedings of the Ocean Drilling Program (Scientific Results), 176.

Dick, H. J. B., Lin, J., and Schouten, H. (2003). An Ultraslow-Spreading Class of Ocean Ridge. *Nature* 426 (6965), 405–412. doi:10.1038/nature02128

Dick, H. J. B., Natland, J. H., Alt, J. C., Bach, W., Bideau, D., Gee, J. S., et al. (2000). A Long *In Situ* Section of the Lower Ocean Crust: Results of ODP Leg 176 Drilling at the Southwest Indian Ridge. *Earth Planet. Sci. Lett.* 179 (1), 31–51. doi:10.1016/s0012-821x(00)00102-3

Dostal, J., and Muecke, G. K. (1978). Trace Element Geochemistry of the Peridotite-Gabbro-basalt Suite from DSDP Leg 37. *Earth Planet. Sci. Lett.* 40 (3), 415–422. doi:10.1016/0012-821x(78)90164-4

Drouin, M., Godard, M., Ildefonse, B., Bruguier, O., and Garrido, C. J. (2009). Geochemical and Petrographic Evidence for Magmatic Impregnation in the Oceanic Lithosphere at Atlantis Massif, Mid-Atlantic Ridge (IODP Hole U1309D, 30°N). *Chem. Geology* 264 (1-4), 71–88. doi:10.1016/j.chemgeo.2009.02.013

Escartin, J., Mével, C., MacLeod, C. J., and McGaig, A. M. (2003). Constraints on Deformation Conditions and the Origin of Oceanic Core Complexes: The Mid-Atlantic Ridge Core Complex at 15°45'N. *Geochem. Geophys.* 4 (8), 1067. doi:10.1029/2002gc000472

Ghent, E. D., Coleman, R. G., and Hadley, D. G. (1979). *Ultramafic Inclusions and Host Alkali Olivine Basalts of the Southern Coastal plain of the Red Sea, Kingdom of Saudi Arabia*. Jeddah: USGS SAUDI ARABIAN PROJECT REPORT, 244.

Goard, M., Awaji, S., Hansen, H., Hellebrand, E., Brunelli, D., Johnson, K., et al. (2009). Geochemistry of a Long *In-Situ* Section of Intrusive Slow-Spread Oceanic Lithosphere: Results from IODP Site U1309 (Atlantis Massif, 30°N Mid-Atlantic Ridge). *Earth Planet. Sci. Lett.* 279 (110-122), 2009. doi:10.1016/j.epsl.2008.12.034

Grove, T. L., and Bryan, W. B. (1983). Fractionation of Pyroxene-Phyric MORB at Low Pressure: An Experimental Study. *Contr. Mineral. Petrol.* 84 (4), 293–309. doi:10.1007/bf01160283

Gurvich, E. G. (2006). "Metalliferous Sediments of the Red Sea," in *Metalliferous Sediments of the World Ocean* (Berlin, Heidelberg: Springer), 127–210.

Habtoor, A., Ahmed, A. H., and Harbi, H. (2016). Petrogenesis of the Alaskan-type Mafic-Ultramafic Complex in the Makkah Quadrangle, Western Arabian Shield, Saudi Arabia. *Lithos* 263, 33–51. doi:10.1016/j.lithos.2016.08.014

Hewitt, A., Salisbury, R., and Wilson, J. (2010). Using Multibeam Echosounder Backscatter to Characterize Seafloor Features. *Sea Technol.* 51, 10–13.

Holm, P. M. (2002). Sr, Nd and Pb Isotopic Composition of *In Situ* Lower Crust at the Southwest Indian Ridge: Results from ODP Leg 176. *Chem. Geology* 184 (3-4), 195–216. doi:10.1016/s0009-2541(01)00364-3

Hübscher, C., and Gohl, K. (2014). "Reflection/Refraction Seismology," in *Encyclopedia of Marine Geosciences* (Dordrecht: Springer), 1–15. doi:10.1007/978-94-007-6644-0_128-1

Jarosewich, E., Nelen, J. A., and Norberg, J. A. (1980). Reference Samples for Electron Microprobe Analysis*. *Geostand. Newslett.* 4 (1), 43–47. doi:10.1111/j.1751-908x.1980.tb00273.x

Koepke, J., Feig, S., and Snow, J. (2005). Late-Stage Magmatic Evolution of Oceanic Gabbros as a Result of Hydrous Partial Melting: Evidence from the Ocean Drilling Program (ODP) Leg 153 Drilling at the Mid-Atlantic Ridge. *Geochem. Geophys.* 6 (2). doi:10.1029/2004gc000805

Ligi, M., Bonatti, E., Bosworth, W., Cai, Y., Cipriani, A., Palmiotto, C., et al. (2018). Birth of an Ocean in the Red Sea: Oceanic-Type Basaltic Melt Intrusions Precede Continental Rupture. *Gondwana Res.* 54, 150–160. doi:10.1016/j.gr.2017.11.002

Lissenberg, J. C., and Dick, H. J. B. (2008). Melt-Rock Interaction in the Lower Oceanic Crust and its Implications for the Genesis of Mid-Ocean ridge basalt. *Earth Planet. Sci. Lett.* 271 (1-4), 311–325. doi:10.1016/j.epsl.2008.04.023

MacLeod, C. J., Escartín, J., Banerji, D., Banks, G. J., Gleeson, M., Irving, D. H. B., et al. (2002). Direct Geological Evidence for Oceanic Detachment Faulting: The Mid-Atlantic Ridge, 15°45'N. *Geol.* 30 (10), 879–882. doi:10.1130/0091-7613(2002)030<0879:dgefod>2.0.co;2

Mevel, C., Gillis, K. M., James, A. F., and Meyer, P. S. (1996). "Hess Deep Rift Valley: Covering Leg 147 of the Cruises of the Drilling Vessel JOIDES Resolution," in Proceedings of the Ocean Drilling Program, San Diego, California, to Balboa Harbor, Panama, Sites 894-895, 22 November 1992 – 21 January 1993 (Scientific results), 147.

Meyer, P. S., Dick, H. J. B., and Thompson, G. (1989). Cumulate Gabbros from the Southwest Indian Ridge, 54°S-7° 16′ E: Implications for Magmatic Processes at a Slow Spreading ridge. *Contr. Mineral. Petrol.* 103 (1), 44–63. doi:10.1007/bf00371364

Middlemost, E. A. K. (1994). Naming Materials in the Magma/Igneous Rock System. *Earth-Science Rev.* 37 (3-4), 215–224. doi:10.1016/0012-8252(94)90029-9

Mitchell, N. C., Ligi, M., Ferrante, V., Bonatti, E., and Rutter, E. (2010). Submarine Salt Flows in the Central Red Sea. *GSA Bull.* 122 (5-6), 701–713. doi:10.1130/b26518.1

Mitchell, N. C., and Park, Y. (2014). Nature of Crust in the Central Red Sea. *Tectonophysics* 628, 123–139. doi:10.1016/j.tecto.2014.04.029

Miyashiro, A., Shido, F., and Ewing, M. (1970). Crystallization and Differentiation in Abyssal Tholeiites and Gabbros from Mid-oceanic Ridges. *Earth Planet. Sci. Lett.* 7 (4), 361–365. doi:10.1016/0012-821x(69)90050-8

Nimis, P. (1999). Clinopyroxene Geobarometry of Magmatic Rocks. Part 2. Structural Geobarometers for Basic to Acid, Tholeiitic and Mildly Alkaline Magmatic Systems. *Contrib. Mineral. Petrol.* 135 (1), 62–74. doi:10.1007/s004100050498

Ozava, K., Meyer, P. S., and Bloomer, S. H. (1991). Mineralogy and Textures of Iron-Titanium Gabbros and Associated Olivine Gabbros from Hole 735B. *Proc. Ocean Drilling Program Scientific Results* 118, 41–73.

Piccardo, G. B., Messiga, B., and Vannucci, R. (1988). The Zabargad Peridotite-Pyroxenite Association: Petrological Constraints on its Evolution. *Tectonophysics* 150 (1-2), 135–162. doi:10.1016/0040-1951(88)90299-5

Putirka, K., Johnson, M., Kinzler, R., Longhi, J., and Walker, D. (1996). Thermobarometry of Mafic Igneous Rocks Based on Clinopyroxene-Liquid Equilibria, 0-30 Kbar. *Contrib. Mineralogy Petrol.* 123 (1), 92–108. doi:10.1007/s004100050145

Ray, D., Misra, S., Banerjee, R., and Weis, D. (2011). Geochemical Implications of Gabbro from the Slow-Spreading Northern Central Indian Ocean Ridge, Indian Ocean. *Geol. Mag.* 148 (3), 404–422. doi:10.1017/s001675681000083x

Rihm, R., Makris, J., and Möller, L. (1991). Seismic Surveys in the Northern Red Sea: Asymmetric Crustal Structure. *Tectonophysics* 198 (2-4), 279–295. doi:10.1016/0040-1951(91)90156-m

Roeser, H. A. (1975). A Detailed Magnetic Survey of the Southern Red Sea. *Geol. JB. D* 13, 143–165.

Schmidt, M., Al-Farawati, R., Al-Aidaroos, A., and Kürten, B. (2013). *RV PELAGIA Cruise Report 64PE350/64PE351*. Kiel: Berichte aus dem Helmholtz-Zentrum für Ozeanforschung Kiel (GEOMAR) 5. doi:10.3289/GEOMAR_REP_NS_5_2012

Schmidt, M., Devey, C. W., and Eisenhauer, A. (2011). *FS POSEIDON Cruise Report P408*. Berichte aus dem Leibniz-Institut für Meereswissenschaften an der ChristianAlbrechts-Universität zu Kiel 46.

Searle, R. C., Cannat, M., Fujioka, K., Mével, C., Fujimoto, H., Bralee, A., et al. (2003). FUJI Dome: A Large Detachment Fault Near 64°E on the Very Slow-Spreading Southwest Indian Ridge. *Geochem. Geophys.* 4 (8). doi:10.1029/2003gc000519

Soesoo, A. (1997). A Multivariate Statistical Analysis of Clinopyroxene Composition: Empirical Coordinates for the Crystallization PT-Estimations. *GFF* 119 (1), 50–60. Stockholm. doi:10.1080/11035899709546454

Stakes, D. S., Shervais, J. W., and Hopson, C. A. (1984). The Volcanic-Tectonic Cycle of the FAMOUS and AMAR Valleys, Mid-Atlantic Ridge (36°47'N): Evidence from Basalt Glass and Phenocryst Compositional Variations for a

Steady State Magma Chamber Beneath the valley Midsections, AMAR 3. *J. Geophys. Res.* 89 (B8), 6995–7028. doi:10.1029/jb089ib08p06995

Stoffers, P., and Ross, D. A. (1974). "Sedimentary History of the Red Sea," in *Initial Reports of the Deep Sea Drilling Program, Initial Reports of the Deep Sea Drilling Project.* Editors P. R. Supko and O.E. Weser (Washing-ton: US Government Printing Office), 849–865. doi:10.2973/dsdp.proc.23.123.1974

Sultan, M., Becker, R., Arvidson, R. E., Shore, P., Stern, R. J., El Alfy, Z., et al. (1992). Nature of the Red Sea Crust: A Controversy Revisited. *Geology* 20 (7), 593–596. doi:10.1130/0091-7613(1992)020<0593:notrsc>2.3.co;2

Tiezzi, L. J., and Scott, R. B. (1980). Crystal Fractionation in a CUmulate Gabbro, Mid-Atlantic Ridge, 26°N. *J. Geophys. Res.* 85 (B10), 5438–5454. doi:10.1029/jb085ib10p05438

Van der Zwan, F. M., Devey, C. W., Augustin, N., Almeev, R. R., Bantan, R. A., and Basaham, A. (2015). Hydrothermal Activity at the Ultraslow- to Slow-Spreading Red Sea Rift Traced by Chlorine in Basalt. *Chem. Geology* 405, 63–81. doi:10.1016/j.chemgeo.2015.04.001